This article has been accepted for publication in a future issue of this journal, but has not been fully edited. Content may change prior to final publication. Citation information: DOI 10.1109/JSTARS.2021.3123326, IEEE Journal of Selected Topics in Applied Earth Observations and Remote Sensing

Determining Suitable Spaceborne SAR Observations and Ground Control Points for Surface Deformation Study in Rugged Terrain with InSAR Technique

Yan Yan and Yong Wang

***Abstract*—We aim to address two primary issues using the multi-temporal (MT) spaceborne SAR observations and InSAR technique to monitor slope stability in rugged terrains. One is how to maximize the observation and application effectiveness based on the geometric distortion in an area of interest (AOI) for determining appropriate ascending- and descending-orbit SAR observations. The other is how to optimize the selection of ground control points (GCPs) to correct orbital phase errors and reference in deriving valid ground surface displacements in the SBAS InSAR analysis. Four criteria were proposed to identify valid GCPs efficiently and effectively. The 2017 Xinmo landslide event, China, was showcased. The tear-away zone was 100% and ~50% distorted when imaged by ascending- and descending-orbit Sentinel-1A/B SAR sensors. The descending SAR datasets were preferred. Then, we identified four spatially dispersed GCP clusters with the selection criteria using the SBAS InSAR technique and 45 descending-orbit MT SAR datasets. One GCP per cluster was chosen. With the four GCPs and SBAS analysis, we successfully detected the stable status in the landslide-free area and the pre-landslide acceleration movement within the tear-away zone. Valid InSAR-derived results have been obtained. In turn, the GCP selection criteria have been validated, and the two issues resolved.**

***Index Terms*—Amplitude dispersion index (ADI); geometric distortion; ground control point (GCP); multi-temporal (MT) observations; phase derivative variance (PDV); SBAS InSAR.**

I. Introduction

THE spaceborne synthetic aperture radar (SAR) uses the side-looking imaging geometry to observe an area of interest (AOI) in Earth observation. With the interferometric SAR (InSAR) technique, one estimates the gradual ground surface deformation utilizing the phase difference information from repeat-orbit SAR observations [1]-[4]. The estimation can capture precursory movements of natural disasters [5]-[9] and surface subsidence [10]-[15]. When the side-looking SAR images rugged terrain, geometric distortion [16], i.e., foreshortening, layover, or shadow, can occur along the line-of-sight (LOS) direction. The distortion affects the effectiveness of using the multi-temporal (MT) SAR observations and InSAR analysis to evaluate the surface deformation. In turn, the critical pre-event (e.g., a landslide precursor) information is affected, and lives can be lost.

Debris of a landslide event in mountainous areas flows along slope downwards. The tear-away zone of a landslide can be any location along a hill. Thus, the zone's location determines the debris flow direction and path. Without knowing the exact location of the zone, the flow direction and route can be uncertain. For example, the downslope direction and path can be on either side when the zone is near the top of a mountain ridge. On the other hand, a SAR observable area in rugged terrain is determined by the interplay of the SAR look angle and the slope and aspect angles of the hill. To the extreme, the slope facing SAR can be foreshortened into only one point when the SAR look angle is equal to the slope angle. The hill facing away from the SAR can be in shadow if the incidence angle is shallow, but the slope is steep. Hence, the quantitative analysis of the interplay is crucial, allowing one to maximize the MT SAR observations' chance to observe the tear-away zone. A better assessment of the debris flow and path is then obtained.

With several hundreds of kilometers above the ground, polar-orbit spaceborne SAR incidence angles from the near to the far range do not vary much. A small range of incidence angle variations does not offer many options to resolve the geometric distortion in rugged terrain. Although SAR repeatedly collects data along ascending and descending orbits, orbit inclinations are fixed, reducing the options further. Thus, even though MT ascending- and descending-orbit SAR observations are available, one needs to quantify the geometric distortions for a given SAR imaging geometry before assessing an AOI's surface deformation. The quantification should conclude that both ascending and descending imaging geometries are suitable, one is preferred to the other, or none is usable.

Ground surface deformation has been investigated by the differential InSAR (DInSAR) technique. Techniques for the simultaneous analyses of large numbers of SAR observations have led to MT InSAR analyses [17]-[21]. MT InSAR (e.g., the persistent scatterers, PS; and small baseline subset, SBAS)

This work was sponsored by the National Natural Science Foundation of China under grant 41771401 to the University of Electronic Science and Technology of China. (*Corresponding author*: *Yong Wang*)

Y. Yan (e-mail: yanyan_river@163.com) is with School of Resources and Environment, University of Electronic Science and Technology of China (UESTC), Chengdu, Sichuan 611731, China and with Center for Information Geoscience, UESTC.

Y. Wang is with Department of Geography, Planning, and Environment, East Carolina University, Greenville, North Carolina 27858, USA (e-mail: wangy@ecu.edu). He has an adjunct position at the School of Resources and Environment, UESTC.

This article has been accepted for publication in a future issue of this journal, but has not been fully edited. Content may change prior to final publication. Citation information: DOI 10.1109/JSTARS.2021.3123326, IEEE Journal of Selected Topics in Applied Earth Observations and Remote Sensing

techniques have significantly improved the measurement accuracy of surface changes. Since pointwise scatterers that remain sufficiently high coherence values at long spatiotemporal baselines are considered in the PS InSAR algorithm, the algorithm's application is limited. As supplementary, the SBAS algorithm exploits pointwise and distributed scatterers with a coherence value higher than a given threshold value, making it more applicable in areas such as mountains where persistent scatterers can be scarce.

A differential interferogram consists of phases related to the ground displacement, decorrelation noise, DEM error, atmospheric delay variation, and satellite orbital error [22], [23]. The SBAS algorithm alleviates the decorrelation effects by a complex multi-looking operation [18], estimates and compensates for topographic artifacts caused by the DEM error, and mitigates the atmospheric effects by a filtering process. Consequently, the orbital phase error (i.e., the phase ramp) remains. The ramp can negatively affect the InSAR surface displacement measurements. For example, the precise orbit determination (POD) data having one standard deviation on the order of 15 cm translates into several centimeters of the LOS displacement when the C-band SAR observations are considered [24]. Thus, the removal or minimization of the phase ramp is sought.

Gourmelen et al. [24] model and remove orbital phase errors from the InSAR data by integrating continuous GPS time series and a physical orbital model. The method explicitly depends on the ground measurements and a priori orbital model. On the other hand, some locations or regions within a study area have no ground surface deformation, and they are used to fit a planar phase ramp in the range and azimuth directions [25]. The fit approach is attractive because it relies on ground control points (GCPs) directly determined from the InSAR data and an implicit model assumption [26].

GCPs, by definition, are stable locations/regions for a period of interest at a study site. Conventionally, the GCPs are visually selected at locations with the interferometric phase consistency in the range and azimuth directions from one interferogram. The method can pose two types of problems. First, visual identification can be subjective and error-prone, and GCPs chosen from one interferogram may have low applicability to the entire InSAR data stack. Fortunately, the phase derivative variance (PDV) quantifies the interferometric phase consistency [27], [28]. The smaller a PDV value is, the higher the consistency. Also, one can overcome the low applicability problem by considering multiple differential interferograms simultaneously to select the GCPs.

The second type of problem is not considering temporal stability. GCPs should be stable for a period of interest at a study site regardless of their usage to correct the phase ramp or derive ground displacement. Thus, a human-made target (e.g., a corner reflector or building) is the desired GCP candidate but is typically unavailable in remote mountainous areas. In addition, the time in an MT-InSAR study can be months or years, and seasonal and annual variations affect radar backscatter. Thus, a GCP should also be situated at a location producing steady radar returns temporally.

Theoretically, the coherence value could be an indicator to identify temporally stable areas. However, the coherence value is a relative value or ratio. A large ratio can result from i) a small numerator value divided by a smaller dominator number or ii) a very large numerator value divided by a large dominator value. In the InSAR coherence coefficient, the denominator value is the product of the amplitudes of the primary image and secondary image at a location. Thus, one can potentially face a wide range of amplitude variations. Furthermore, to assess the stability through the entire observation period, one needs to co-register all SAR images in the SAR data stack. The number of possible combinations can be prohibitive, and the coherence analysis approach to evaluate the temporal stability is inefficient. Alternatively, the amplitude dispersion index (ADI) [17] directly utilizes the SAR amplitudes to assess the temporal stability on a pixel-by-pixel basis, and the ADI approach is effective and efficient [17]. A small ADI value at a location indicates its high stability.

Georeferencing SAR datasets in the MT-InSAR analysis is a must operation before the GCP selection. Although a root mean square error (RMSE) can be statistically obtained at a sub-pixel level, the rectification is achieved at the smallest increment of one row or column. It can be concerned if an individual location or an isolated pixel is selected as a GCP. Thus, one should choose a GCP from at least a patch of 2×2 pixels, with all four being GCPs. A patch size of 3×3 or larger is even better but may become impossible due to the interplay of the SAR spatial resolution and local topography. In particular, the SAR resolution is moderate and the terrain rugged. Furthermore, GCPs should be spatially dispersed within the study area such that the phase ramp correction and InSAR-derived outcomes are not dictated by a single GCP or a GCP cluster.

Based on the discussion above, two primary research questions are i) how to maximize the observation and application effectiveness based on the SAR geometric distortion for determining appropriate ascending- and descending-orbit SAR imaging geometries; and ii) how to optimize the selection of GCPs to correct orbital phase errors and reference to derive valid ground surface displacements in the SBAS InSAR analysis. To address them, we develop a selection procedure for the SAR observations and GCPs. Particularly, the geometric distortion impact within the landslide-impacted area imaged by an ascending- and descending-orbit SAR is quantified. Then, the number of GCPs as a function of the PDV and ADI threshold values and the GCP spatial distribution and patches are studied. One threshold value for the PDV and another for the ADI are determined, and GCPs are selected. To validate the proposed GCP selection method, we apply the GCPs to the SBAS InSAR analysis and analyze the surface deformation through time at the landslide-free area and the tear-away zone.

This article has been accepted for publication in a future issue of this journal, but has not been fully edited. Content may change prior to final publication. Citation information: DOI 10.1109/JSTARS.2021.3123326, IEEE Journal of Selected Topics in Applied Earth Observations and Remote Sensing

II. Methodology

A. Geometric Distortion in Rugged Terrain Imaged by Side-looking SAR

A polar-orbit spaceborne SAR with an imaging geometry of right-and-downward looking is shown in **Fig. 1(a)** with the radar heading angle of α_h and the radar incidence angle of θ. The AOI has aspect angle β and slope angle s, and vector k_1 is the normal direction of the slope. When the SAR travels along the ascending orbit [**Fig. 1(b)**], the slope towards the SAR predominantly faces the west. The slope facing the descending-orbit SAR is equivalently towards the east, as shown in **Fig. 1(c)**.

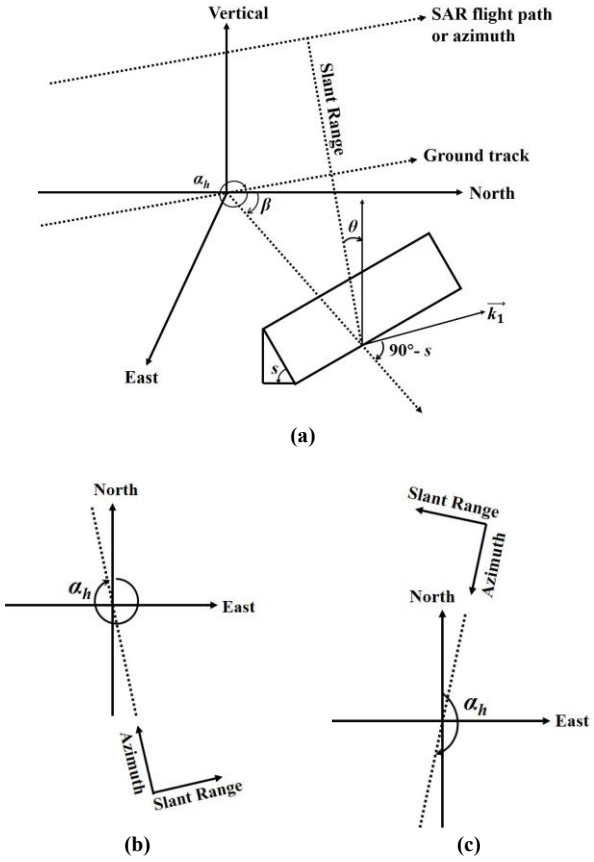

Fig. 1. A polar-orbit SAR with an imaging geometry of a right-and-downward looking. **(a)** Radar heading angle α_h and radar incidence angle θ are illustrated. The AOI has aspect angle β and slope angle s. Vector k_1 is perpendicular to the slope. **(b)** An ascending-orbit imaging geometry, and **(c)** a descending-orbit imaging geometry.

In **Fig. 1**, the slope faces the SAR if

$$\beta = \begin{cases} > \alpha_h - 180^\circ \\ < \alpha_h \end{cases} \tag{1}$$

For a slope facing away from the radar,

$$\beta = \begin{cases} \geq 0 \\ \leq \alpha_h - 180^\circ \end{cases} \text{ or } \begin{cases} \geq \alpha_h \\ < 360^\circ \end{cases} \tag{2}$$

In rugged terrain facing towards the radar, the foreshortening occurs when s is less than θ. The layover happens if s is $\geq \theta$. Once $(s + \theta)$ for terrain facing away from the radar is greater than 90°, shadow occurs. There is no radar return from the shadow or terrain. In summary, one expresses the three types of distortion as

$$\begin{aligned} &\text{Foreshortening: If } ((\alpha_h - 180^\circ) < \beta < \alpha_h \text{ and } s < \theta) \\ &\text{Layover: If } ((\alpha_h - 180^\circ) < \beta < \alpha_h \text{ and } s \geq \theta) \\ &\text{Shadow: } \begin{cases} \text{If } (0 \leq \beta \leq (\alpha_h - 180^\circ) \text{ and } (s+\theta) > 90^\circ) \\ \alpha_h \leq \beta < 360^\circ \text{ and } (s+\theta) > 90^\circ) \end{cases} \end{aligned} \tag{3}$$

B. GCP Selection in the MT-InSAR Analysis

A GCP should be at locations with wrapped phase consistency. The consistency can be evaluated by combining the partial derivative variances in azimuth (x) and slant range (y) directions [27], [28]. Within an $n \times n$ window, the PDV [27], [28] at the center of the window or (i, j) is

$$\text{PDV}_{i,j,k} = \frac{\sqrt{\sum_{l,m=1}^{n} \Delta x_{l,m} - \overline{\Delta x_{l,m}}^{\,2}} + \sqrt{\sum_{l,m=1}^{n} \Delta y_{l,m} - \overline{\Delta y_{l,m}}^{\,2}}}{n \cdot n} \tag{4}$$

where $\text{PDV}_{i,j,k}$ is the PDV at location (x, y) derived from the k-th interferogram. $\Delta x_{l,m} = \varphi_{l,m} - \varphi_{l-1,m}$ is the partial derivative of the wrapped phase in the x-direction and $\Delta y_{l,m} = \varphi_{l,m} - \varphi_{l,m-1}$ the partial derivative in the y-direction. $\varphi_{i,j}$ is the wrapped phase at (i, j). $\overline{\Delta x_{l,m}}$ is the average of $\Delta x_{l,m}$ and $\overline{\Delta y_{l,m}}$ the average of $\Delta y_{l,m}$ within the $n \times n$ window. A small $\text{PDV}_{i,j,k}$ suggests that the phase is consistent at location (i, j) of the k-th interferogram.

There are typically a large number of interferograms in an SBAS InSAR analysis. We randomly select a subset of o interferograms to avoid the overall phase consistency dictated by a single interferogram. The phase consistency at location (i, j) or $PC_{i,j}$ is evaluated as

$$PC_{i,j} = \begin{cases} 1 \text{ if } \text{PDV}_{i,j,k} \leq PDV_s & \text{for } k = 1, 2, \ldots, \text{and } o \\ 0 & \text{Otherwise} \end{cases} \tag{5}$$

where 1 stands for consistency and 0 for inconsistency. PDV_s represents a PDV threshold value that is small and is empirically determined. As o increases, the number of 1s within an AOI generally decreases.

To quantify the temporal stability at a location, we use the ADI [17] or

$$\text{ADI} = \sigma / \mu \tag{6}$$

This article has been accepted for publication in a future issue of this journal, but has not been fully edited. Content may change prior to final publication. Citation information: DOI 10.1109/JSTARS.2021.3123326, IEEE Journal of Selected Topics in Applied Earth Observations and Remote Sensing

where μ and σ are the mean and standard deviation of the amplitude values of georeferenced MT images in the SAR image stack. A small ADI indicates that a location has consistent radar returns through time or it is temporally steady. Then, a place is a potential GCP if its ADI is $\leq ADI_s$, with ADI_s being a small and empirically determined threshold value.

Finally, after considering the GCP's spatial distribution pattern within the study area and the existence of 2×2 GCP patches, one completes the iterative GCP selection process.

III. Study Area and Datasets

On 24 June 2017, a landslide event occurred near the Xinmo village (32°03′ 59.42″ N, 103°39′ 1.93″ E), Mao County, Sichuan Province, China. A study area of ~10×10 km is selected around the landslide site. **Fig. 2(a)** is the area's digital elevation model (DEM), indicating the rugged terrain and significant elevation difference. **Fig. 2(b)-(c)** are Landsat-8 images acquired before and after the event. The landslide mass was initiated from a tear-away zone, about 370 m along the slope and 380 m transversely. The debris flow direction and path were roughly from the northeast to the southwest. The landslide scar, ~3 km long along the slope, is shown within a polygon. The affected village was along the Songpinggou River banks and near the toe of the scar.

Four primary reasons exist to choose the site and landslide event. First, the rugged terrain susceptible to geometric distortions was imaged by the ascending- and descending-orbit side-looking Sentinel-1 SAR. Second, there are few human-made structures due to a remote rural area, and the chance that the structures are possible GCPs is slim. Third, the landslide-affected area outlined by a polygon is large and easily distinguishable with the moderate resolution satellite data [**Fig. 2(b)-(c)**]. A landslide-free area and a tear-away zone are marked in **Fig. 2(c)**. Both are used to validate the proposed procedure to determine suitable spaceborne SAR observations and GCPs for surface deformation study in rugged terrain with the InSAR technique. Fourth, InSAR studies about the 2017 landslide event have been published [29]-[32]. The inter-comparison is possible.

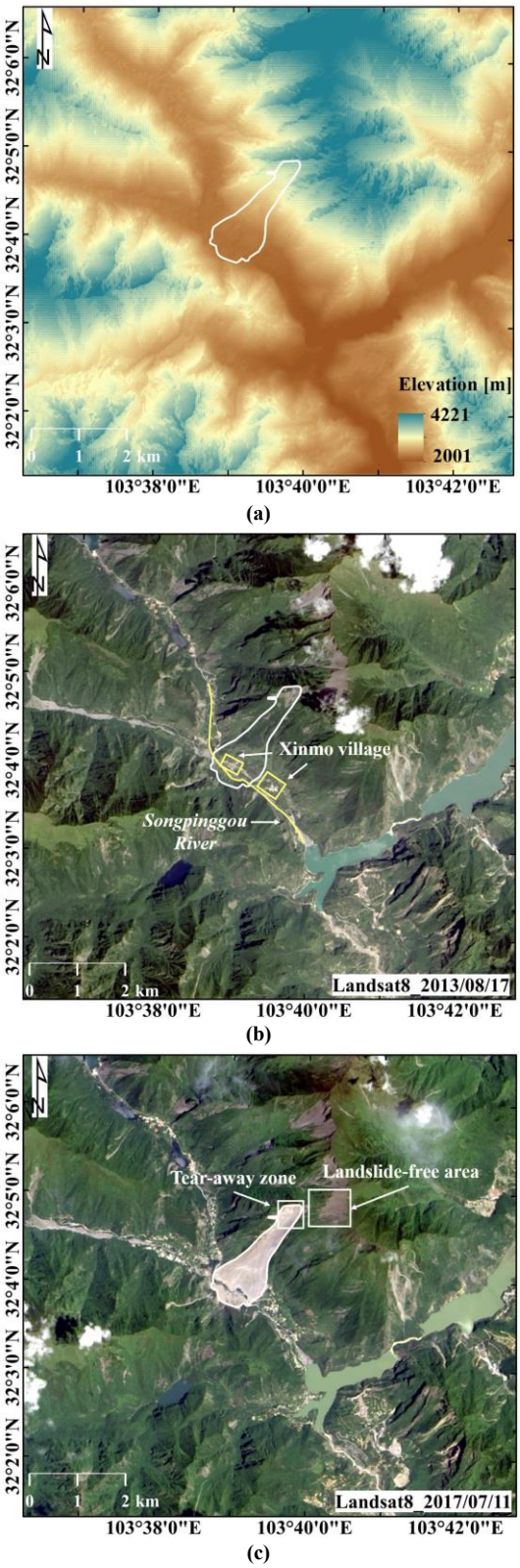

Fig. 2. **(a)** The DEM of the study area centered around the Xinmo landslide site, Mao County, Sichuan Province, China. Landsat-8 optical images before **(b)** and after **(c)** the 2017 event. The white polygon outlines the landslide affected area.

This article has been accepted for publication in a future issue of this journal, but has not been fully edited. Content may change prior to final publication. Citation information: DOI 10.1109/JSTARS.2021.3123326, IEEE Journal of Selected Topics in Applied Earth Observations and Remote Sensing

At the Alaska Satellite Facility (ASF) data portal, we downloaded Sentinel-1A/B single look complex (SLC) datasets acquired along ascending and descending orbits from October 2014, when the SAR data became available, to June 2017, before the landslide event. There are 46 ascending-orbit images from 14 October 2014 to 12 June 2017 and 45 descending-orbit images from 9 October 2014 to 19 June 2017. All are in the interferometric wide swath (IW) mode. The spatial resolution is 5 (slant range) × 20 (azimuth) m. The SAR heading angle is 347.2° for the ascending orbit and 192.8º for the descending one. We downloaded the Precise Orbit Ephemerides (POE) for Sentinel-1 SAR (https://s1qc.asf.alaska.edu/aux_poeorb/) of each SAR image and performed the updates accordingly before the SBAS InSAR analysis. The DEM at 1-arcsecond spacing was obtained from the same ASF portal and used to derive the topographic parameters (i.e., slope and aspect angles) and remove topographic phases in the interferometric process.

IV. Results And Analyses

A. Geometric Distortions

With Sentinel-1 SAR imaging geometry along ascending and descending orbits (**Fig. 1**), slopes face the ascending-orbit SAR observations when their aspect angles range from 167.2° to 347.2°. Slopes face the descending-orbit SAR observations if aspect angles are between 12.8° and 192.8°. In the study area, the radar incidence angle is near 42.1° for the ascending-orbit SAR observations and ~40.3° for the descending-orbit data. Then, with (3) and DEM, foreshortening, layover, and shadow were derived. **Fig. 3** shows the results. Since the landslide-affected area is mainly along the northeast-to-southwest slope, the landslide area within the polygon faces the ascending-orbit SAR. The entire area is nearly affected by foreshortening [**Fig. 3(a)**]. Meanwhile, the area facing away from the descending-orbit SAR is almost not distorted [**Fig. 3(b)**]. Thus, the descending-orbit SAR observations are preferred.

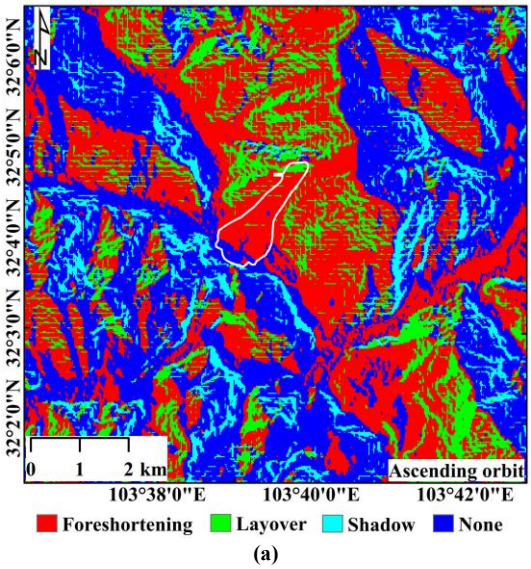

(a)

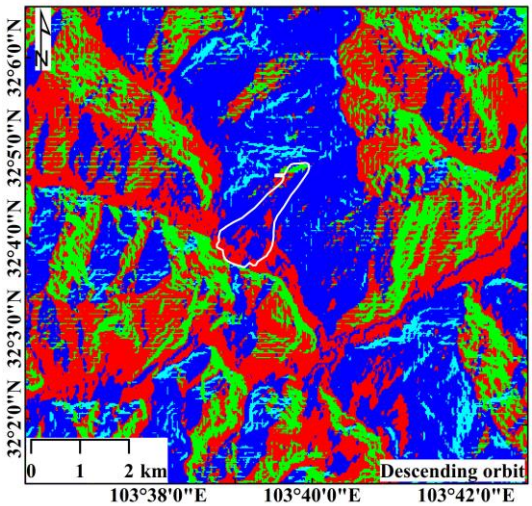

(b)

Fig. 3. Geometric distortions as Sentinel-1 SAR observes the study area along ascending **(a)** and descending **(b)** orbits.

In the landslide study, particularly in providing an imminent alert before the slide, one needs to assess rapid surface movement or a precursor in the tear-away zone. With the MT SAR observations and InSAR technique being the primary means, geometric distortions in the zone should be minimal. Thus, the probability that the InSAR-derived results are valid is high, and the opportunity to catch the precursor is maximized. Within the tear-away zone of the 2017 landslide, numbers of pixels affected by foreshortening, layover, and shadow were quantified. The results are tabulated in TABLE I. At a ground-range resolution of 20×20 m, a total of 309 pixels exists in the zone. With ascending-orbit observations, 143 are affected by foreshortening and 166 by the layover. The distortions impact the entire zone. With descending-orbit observations, pixels affected by the foreshortening, layover, and shadow are 153 or 49.5% of the entire zone. The non-distortion pixels are 156 or 50.5%. Therefore, the descending-orbit imaging geometry is chosen in identifying the landslide precursor. Incidentally, Sentinel-1 descending SAR datasets were used [29]-[32], but ascending-orbit datasets were not considered. The quantitative results of the geometric distortion analysis here offer the reason and answer.

TABLE I
NUMBERS OF PIXELS WITHIN THE TEAR-AWAY ZONE AFFECTED BY FORESHORTENING, LAYOVER, AND SHADOW FOR THE ASCENDING- AND DESCENDING-ORBIT SAR OBSERVATIONS. THE TOTAL NUMBER OF PIXELS IS 309

Orbit	Foreshortening	Layover	Shadow	None
Ascending	143 (46.3%)	166 (53.7%)	0 (0.0%)	0 (0.0%)
Descending	33 (10.7%)	105 (34.0%)	15 (4.8%)	156 (50.5%)

This article has been accepted for publication in a future issue of this journal, but has not been fully edited. Content may change prior to final publication. Citation information: DOI 10.1109/JSTARS.2021.3123326, IEEE Journal of Selected Topics in Applied Earth Observations and Remote Sensing

B. GCP Selection

After processing 45 descending-orbit SAR datasets, we formed 155 interferograms based on selecting InSAR pairs with perpendicular baseline less than 200 m and temporal separations less than 96 days to get better coherence. The interferograms were multi-looked with 4 in range and 1 in azimuth to reduce the decorrelation noise. Topographic and orbit geometry phase delays were estimated and removed from the interferogram using the external DEM and POD POE data. To ensure the unwrapping successfully, we masked out areas with coherence values less than 0.3. Since the tear-away zone was located at the middle-upper part of the slope [**Fig. 2(c)**] and was characterized by small terrain relief, the Itoh condition [28] was met. Hence, each interferogram was satisfactorily unwrapped using the Delaunay minimum cost-flow (MCF) method. The GCP selection procedure is detailed next.

We selected o interferograms randomly and generated o PDV images using (4) with window size n = 3. The interferometric phase consistency at each location was evaluated using (5), creating a binary image. After aligning 45 amplitude images and using (6), an ADI image was generated. **Fig. 4** shows the number of potential GCPs varying with PDV_s and ADI_s, with o being 20. If ADI_s is ≤ 0.11 or PDV_s ≤ 0.02, the number is zero. When ADI_s or PDV_s increases, the GCP number increases. Once ADI_s reaches 0.25 and PDV_s 0.20, the number is over 1,000 or too many. An appropriate PDV_s should be between 0.02 and 0.20. The GCP number may not increase much for a given PDV_s value if ADI_s is ≥ 0.25. Thus, an ADI_s should be roughly from 0.11 to 0.25.

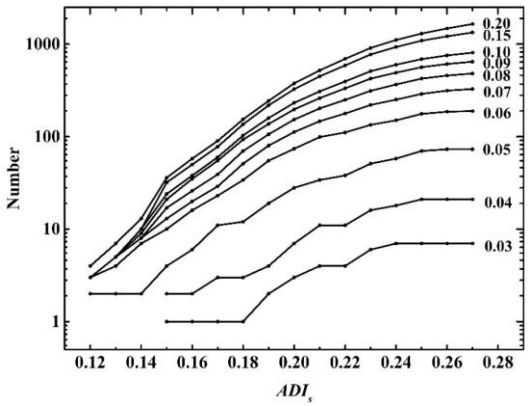

Fig. 4. The y-axis is the number of possible GCPs determined by PDV_s and ADI_s, and the x-axis is ADI_s. An individual PDV_s value is labeled at the right end of each curve.

Next, changing PDV_s from 0.02 to 0.20 and ADI_s from 0.11 to 0.25, coupled with a sieve operation using a 2×2 mesh, we studied the number and spatial distribution of GCPs in the study area. As PDV_s increased to 0.14 and ADI_s to 0.20, four GCP clusters were found. They are dispersed, as shown in **Fig. 5(a)**. Within clusters C_1–C_3, there are at least three GCP patches of 2×2 pixels. One 2×2 patch exists in cluster C_4. Consequentially, the threshold value for $PC_{i,j}$ is found, or PDV_s is 0.14. An ADI threshold value is also determined or ADI_s = 0.20. The total number of GCPs is 54. It should be noted that when 21 randomly selected PDVs were used to produce the binary $PC_{i,j}$ image with PDV_s = 0.14, C_3 and C_4 disappeared. As shown in **Fig. 5(b)**, the GCPs are not dispersed compared to those in **Fig. 5(a)**. Therefore, o of 20 is determined. Also, only one 3×3 GCP patch existed in cluster C_3 if a 3×3 mesh was used in the sieve operation.

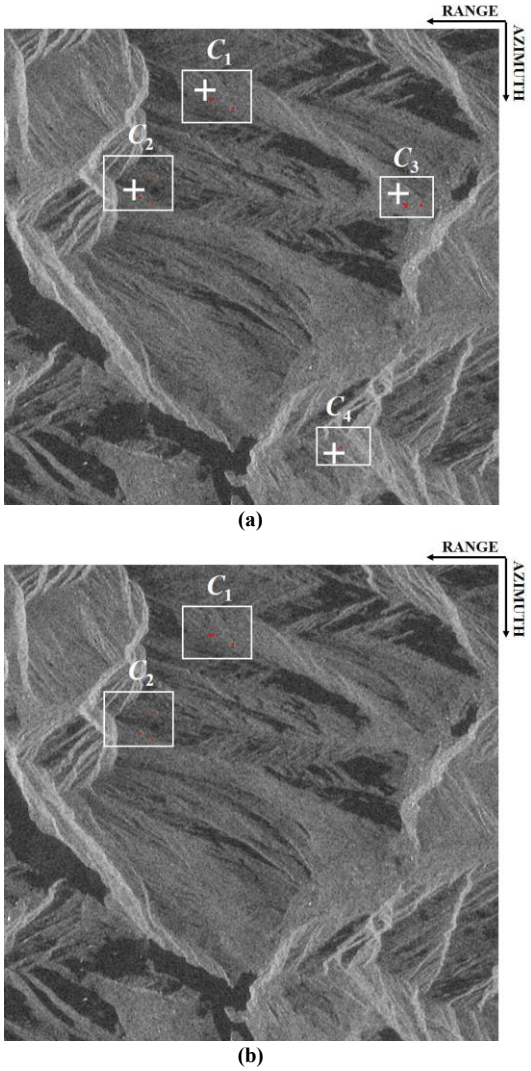

Fig. 5. GCPs (red dots) within the study area are identified with PDV_s = 0.14 and ADI_s = 0.20. The GCPs are superimposed onto the amplitude image in the slant range and azimuth coordinates. The number of interferograms is 20 for **(a)** and 21 for **(b)**.

C. Validation of the Proposed GCP Selection Method

Fig. 6 shows the differential interferogram relevant to the Sentinel-1 SAR data pair acquired on 29 August 2015 and 16 October 2015. **Fig. 6(a)** is the interferogram achieved by using only the POD POE data. There are orbital phase artifacts (e.g.,

This article has been accepted for publication in a future issue of this journal, but has not been fully edited. Content may change prior to final publication. Citation information: DOI 10.1109/JSTARS.2021.3123326, IEEE Journal of Selected Topics in Applied Earth Observations and Remote Sensing

in black rectangles), mimicking the topographic phase patterns and exhibiting periodic color changes.

Next, we selected four GCPs with one GCP per cluster, avoiding the phase ramp correction dictated by a single GCP or GCP cluster. Each GCP is shown as a white plus [**Fig. 5(a)**]. A ramp plane was fit over the GCPs and subtracted from the differential interferograms in the InSAR data stack. **Fig. 6(b)** is the interferogram after the phase ramp correction. The refined phases, such as within the rectangles, are of consistent colors, indicating no deformation. The results conform with the actual stability in these regions [e.g., **Fig. 2(b)-(c)**]. Thus, the phase ramp correction is necessary, and the correction based on the selected GCPs is valid.

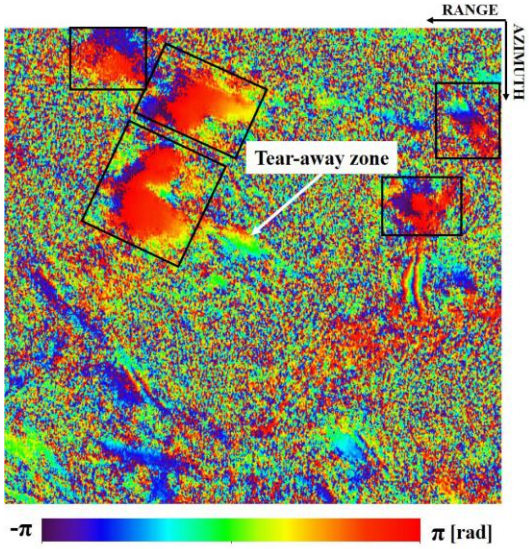

(a)

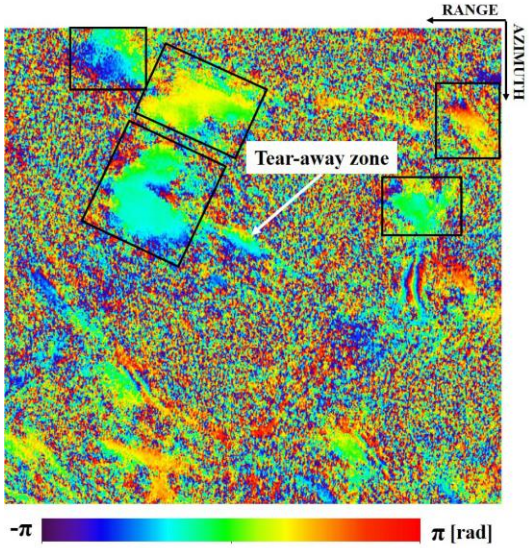

(b)

Fig. 6. The phase ramp correction of the differential interferogram with the August 29, 2015–October 16, 2015 data pair. **(a)** After using the POD POE data and **(b)** after applying the phase ramp correction based on the four dispersive GCPs. Orbital phase artifacts within black rectangles are apparent in **(a)** but effectively mitigated in **(b)**.

Then, the re-unwrapping and atmospheric artifacts correction procedures embedded in the typical SBAS InSAR software are carried out with the refined interferograms. The mean velocity (mm/year) is resolved via the method of singular value decomposition (SVD). The entire speed range was color-coded into six categories, and the results are shown in **Fig. 7**. Because locations with coherence lower than 0.3 were masked out in the phase unwrapping procedure, the points are mainly distributed along the valley and around the landslide-free and landslide areas [**Fig. 2(c)**]. In **Fig. 7**, a positive value corresponds to a movement toward the SAR, while a negative value is the opposite. The results indicated that the area above the zone was stable, but the tear-away zone was not.

We next derived the displacement relative to the four GCPs. The central difference method calculated the velocity (mm/day) between two adjacent SAR observations. The velocity is based on the inverted displacement values to interpret the acceleration process directly. The surface deformation patterns were quantitatively analyzed within the landslide-free area and the tear-away zone.

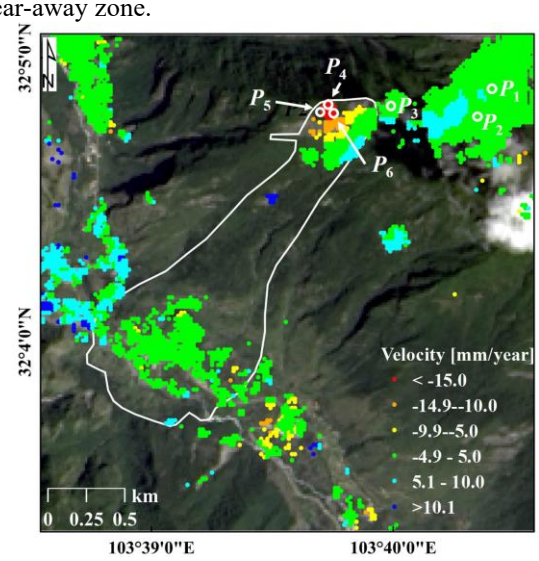

Fig. 7. The mean velocity (mm/year) map derived from the SBAS InSAR analysis. Six samples with three (P_1–P_3) in the landslide-free area and three (P_4–P_6) in the tear-away zone are located.

The landslide-free area: The displacement and velocity time series were extracted at locations P_1, P_2, and P_3 in **Fig. 7**. **Fig. 8** shows the results, where red, green, and blue curves correspond to P_1, P_2, and P_3, respectively. The three curves' displacements change from –2 to 16 mm from 2014 to 2017 with an average of 5.6 mm [**Fig. 8(a)**]. The velocity fluctuates around zero, varying between −0.3 and ~0.4 mm/day [**Fig. 8(b)**]. Near the landslide event date of June 2017, the displacement and velocity values were insignificant, or no accelerated movement occurred. The outcomes are anticipated

This article has been accepted for publication in a future issue of this journal, but has not been fully edited. Content may change prior to final publication. Citation information: DOI 10.1109/JSTARS.2021.3123326, IEEE Journal of Selected Topics in Applied Earth Observations and Remote Sensing

for the landslide-free or stable area. Thus, valid InSAR results are derived with the selected GCPs, indicating the validity of the proposed GCP selection method.

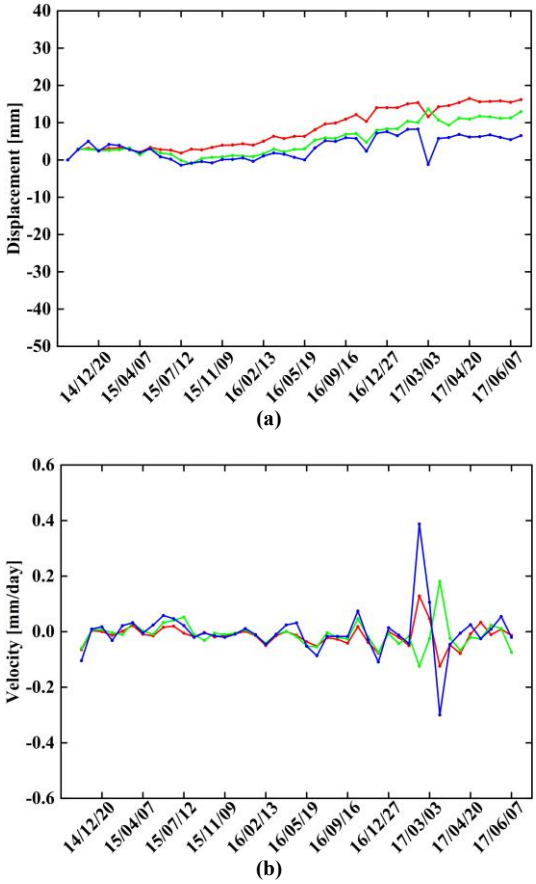

Fig. 8. The SBAS-derived **(a)** displacement and **(b)** velocity time series at locations P_1 (red), P_2 (green), and P_3 (blue). The three locations are inside the landslide-free area. The label on the x-axis is YY/MM/DD.

The tear-away zone: The displacement and velocity values at locations P_4, P_5, and P_6 (**Fig. 7**) were extracted. The time series are separately shown in red, green, and blue in **Fig. 9**. The displacement moved downwards from October 2014 to June 2017 [**Fig. 9(a)**], and the velocity changed gradually from October 2014 to March 2017 [**Fig. 9(b)**]. Then, the displacement and velocity increased significantly till the landslide event on 24 June 2017. The landslide precursor has been successfully captured.

It should be noted that the acceleration started in April 2017 in [29], [32]. A sliding acceleration was revealed before the landslide event [30], and an abrupt acceleration after May 2017 was detected [31]. Those studies and ours identified similar accelerated patterns before the landslide event. Thus, the GCP selection method is also validated in the tear-away zone.

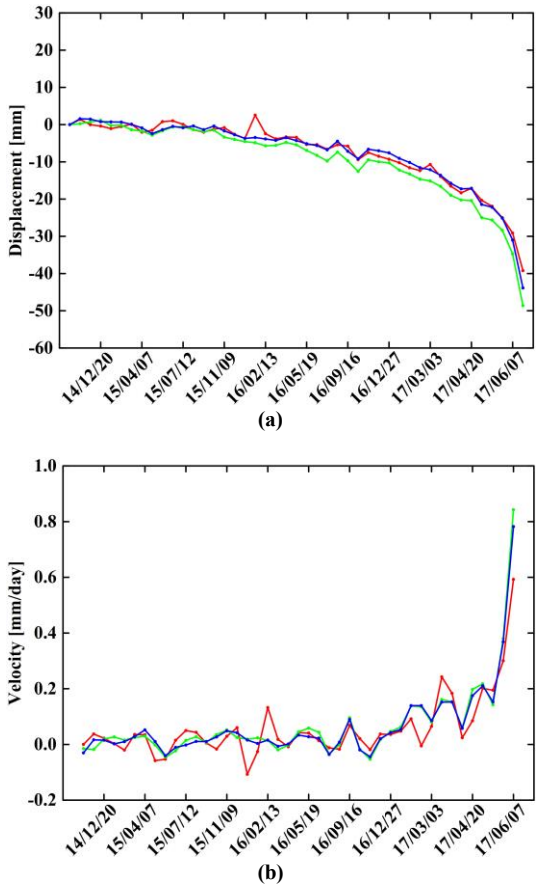

Fig. 9. The SBAS-derived **(a)** displacement and **(b)** velocity time series at locations P_4 (red), P_5 (green), and P_6 (blue) within the tear-away zone.

V. Discussions

A. GCP Validity and Significance of GCPs' Spatial Dispersion

As shown in **Fig. 5(a)**, there are multiple 2×2 GCP patches in clusters C_1–C_3. To understand the importance of the spatial dispersion of GCPs on the InSAR-derived results, we selected three GCPs from three patches of C_1, one GCP per patch. The three GCPs were applied to the SBAS InSAR analysis. The displacement and velocity time-series at the exact three locations P_4, P_5, and P_6 in the tear-away zone were extracted and shown as solid red, green, and blue curves in **Fig. 10**. The displacements of P_4, P_5, and P_6 have downward trends between 2014 and June 2017 [**Fig. 10(a)**]. The velocities fluctuate around 0 mm/day [**Fig. 10(b)**]. As of 19 June 2017, the cumulative displacement at the three locations averaged to near –60 mm. The velocity of P_4, P_5, and P_6 averaged to be about 0.8 mm/day.

Similarly, three GCPs, phase ramp correction, re-unwrapping, atmospheric artifacts correction, and displacement and velocity extractions were repeated for C_2 and C_3. The results for C_2 are shown as dashed curves and for C_3

This article has been accepted for publication in a future issue of this journal, but has not been fully edited. Content may change prior to final publication. Citation information: DOI 10.1109/JSTARS.2021.3123326, IEEE Journal of Selected Topics in Applied Earth Observations and Remote Sensing

dotted ones in **Fig. 10**. The three-dashed curves of the displacement time series were around –20 mm until about the end of March 2017 in **Fig. 10(a)**. The time-series velocity values were near 0 mm/day [**Fig. 10(b)**]. Then, both values increased significantly. Also, the three-dotted curves were around 0 mm until about the end of March 2017 in **Fig. 10(a)**. The velocity values were near 0 mm/day [**Fig. 10(b)**]. Then, the displacement and velocity values increased substantially. In short, the accelerated movement patterns near the landslide event were evident in all three cases that different sets of GCPs have been used in InSAR analyses. The selected GCPs are valid again.

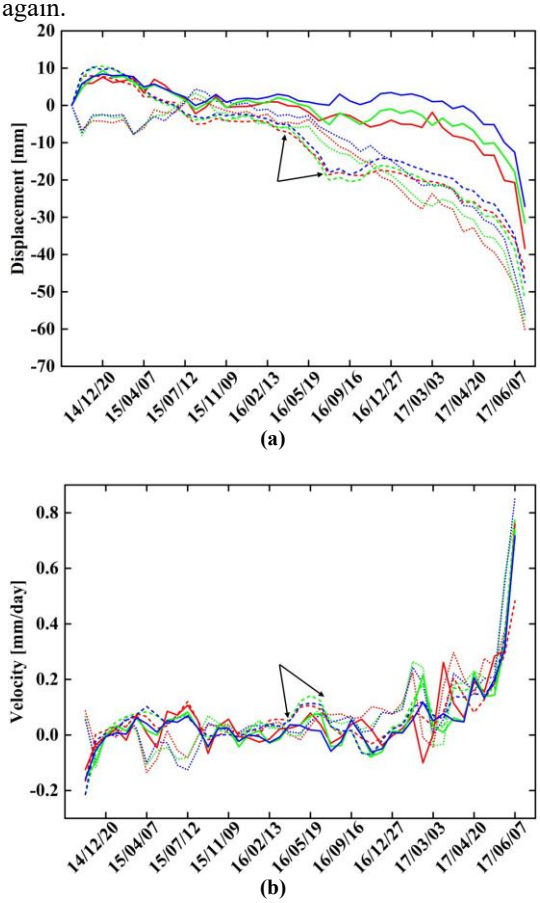

Fig. 10. At locations P_4, P_5, and P_6 in the tear-away zone, the SBAS-derived displacement **(a)** and velocity **(b)** time series. The solid, dashed, and dotted lines relate to the InSAR outcomes using three GCPs from C_1, C_2, and C_3 in **Fig. 5(a)**, respectively. The red, green, and blue lines separately correspond to locations P_4, P_5, and P_6.

In comparison, the displacement curves in **Fig. 9(a)** and **Fig. 10(a)** and the velocity curves in **Fig. 9(b)** and **Fig. 10(b)** have similar patterns overall. However, the displacement and velocity time-series patterns in **Fig. 9** are much smoother than those in **Fig. 10**. To argue the preference of dispersed GCPs, we closely examined the solid curves in **Fig. 9** and dashed curves in **Fig. 10**. Between February and May 2016, pointed by a pair of black arrows in **Fig. 10**, noticeable displacement was observed and continuously increased from about −4 to −18 mm [**Fig. 10(a)**]. The corresponding velocity continuously accelerated from ~0.04 to 0.1 mm/day [**Fig. 10(b)**]. One may conclude that the landslide precursor is captured, and an incoming landslide event warning is issued. If so, the mis-capture of the precursor and a false alarm occurs because the Xinmo landslide happened on 24 June 2017. Therefore, although the selected GCPs were valid and with them, the landslide precursor near June 2017 has been revealed in **Figs. 9** and **10**, one should use spatially dispersed GCPs in a surface deformation study. As shown here, one will be more confident about the InSAR outcomes since the chance to obtain possible biased products using GCPs from one single GCP cluster decreases.

B. Necessity in Selecting GCPs with Both PDV and ADI

After a sieve operation with a 2×2 mesh, possible GCPs with PDV_s of 0.14 are shown in **Fig. 11(a)**. There are at least six clusters, and the total number of GCPs is 1,601. Similarly, multiple GCP clusters exist satisfying $ADI_s = 0.20$ [**Fig. 11(b)**]. There are 266 GCPs. In comparison, the number of GCPs in **Fig. 5(a)** is 54. It is about 3.4% in **Fig. 11(a)** and ~20.3% in **Fig. 11(b)**. The combined use of PDV ≤ PDV_s and ADI ≤ ADI_s reduces the number of GCPs significantly, improving the efficiency of selecting valid GCPs, as shown next.

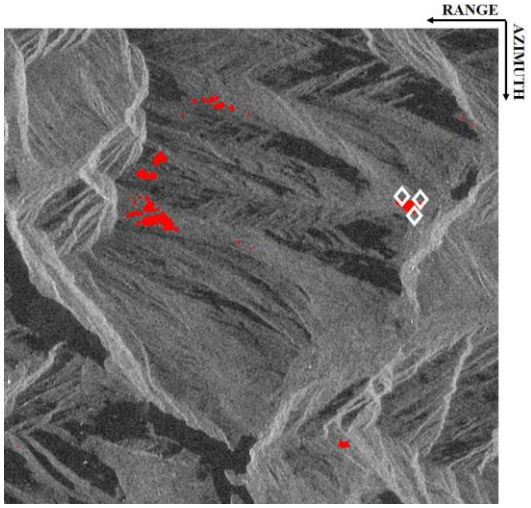

(a)

This article has been accepted for publication in a future issue of this journal, but has not been fully edited. Content may change prior to final publication. Citation information: DOI 10.1109/JSTARS.2021.3123326, IEEE Journal of Selected Topics in Applied Earth Observations and Remote Sensing

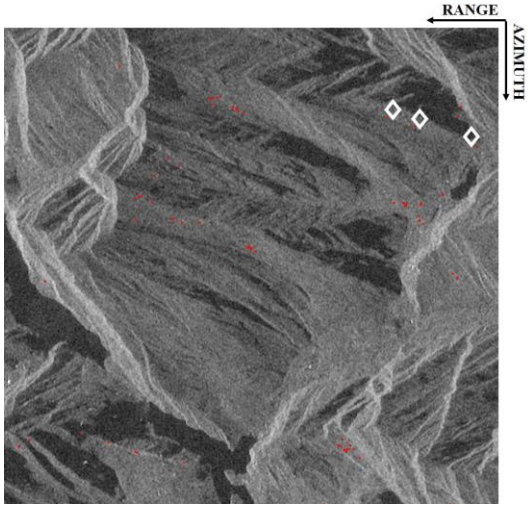

(b)

Fig. 11. GCPs (red dots) are identified by **(a)** PDV ≤ 0.14 and **(b)** ADI ≤ 0.20. Three GCPs are selected with $PC_{i,j} = 1$ and ADI > 0.20 in **(a)**, and three GCPs with $PC_{i,j} = 0$ and ADI ≤ 0.20 in **(b)**. White diamonds denote the selected GCPs.

GCPs in **Fig. 5(a)** were selected with PDV ≤ 0.14 and ADI ≤ 0.20, and GCPs in **Fig. 11(a)** with PDV ≤ 0.14 only. The GCPs of the former are a subset of the GCPs of the latter. Then, among GCPs in **Fig. 11(a)**, we selected three GCPs of PDV ≤ 0.14 and ADI > 0.20 and marked them as white diamonds. The three GCPs were applied to the SBAS InSAR analysis with identical parameters and procedures used in §IV.C. The displacement and velocity time series were extracted at P_4, P_5, and P_6 (**Fig. 7**), and the results are shown as solid red, green, and blue lines in **Fig. 12**. The displacement curves in **Fig. 12(a)** exhibit downward movements overall. However, before the landslide event date, the movement trends were reversed. As shown in **Fig. 12(b)**, two of the three-speed values became even negative. The pre-landslide acceleration evaluated by the displacement or velocity values was not evident compared to the InSAR outcomes in **Figs. 9** and **10**. The relaxed ADI requirement in the GCP selection is attributed to the cause that the temporal stability decreases with the ADI increase. In turn, the InSAR analysis is adversely affected, missing the landslide precursor. The missingness was reported in [33].

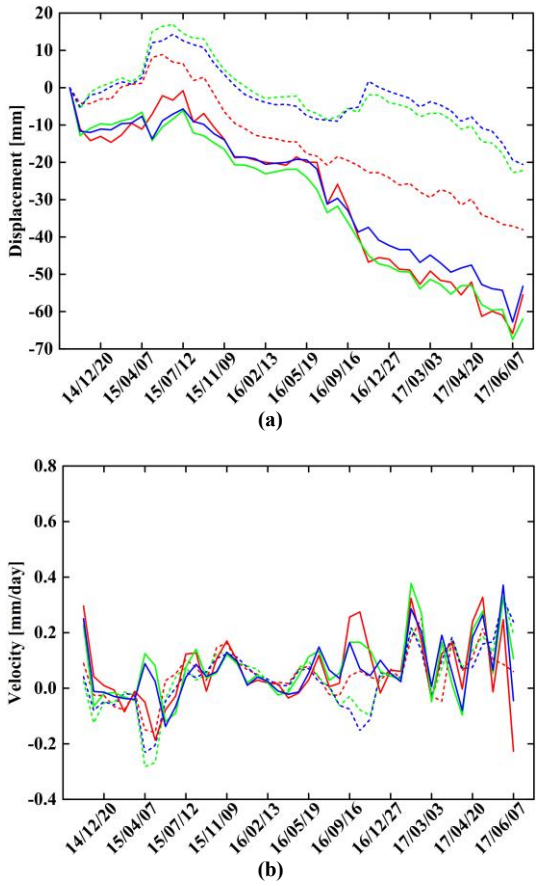

Fig. 12. At locations P_4, P_5, and P_6 in the tear-away zone, the SBAS-derived **(a)** displacement and **(b)** velocity time series. Three solid curves relate to the InSAR outcomes using three GCPs in **Fig. 11(a)**, and three dashed curves correspond to the InSAR results using three GCPs in **Fig. 11(b)**. The red, green, and blue lines, separately, correspond to curves of locations P_4, P_5, and P_6.

Since GCPs in **Fig. 11(b)** were selected with ADI ≤ 0.20, the GCPs in **Fig. 5(a)** are also a subset of GCPs in **Fig. 11(b)**. Among the GCPs in **Fig. 11(b)**, we chose three GCPs with PDV > 0.14 and ADI ≤ 0.20. Doing so ensures that each selected GCP here is not a GCP in **Fig. 5(a)**. Again, three GCPs or white diamonds in **Fig. 11(b)** were applied to the SBAS InSAR analysis with identical parameters and procedures used in §IV.C, producing the displacement and velocity time series of locations P_4, P_5, and P_6 in the tear-away zone. **Fig. 12** shows the results as dashed red, green, and blue lines. The displacements reveal downward trends from October 2014 to June 2017 in **Fig. 12(a)**. An accelerated displacement near the landslide event date may not exist because the velocity at the three locations near the event date fluctuates irregularly. Compared to the selection requirement identifying the GCPs in **Fig. 5(a)**, the PDV requirement is loosened in selecting the GCPs in **Fig. 11(b)**, and the phase consistency requirement of the twenty PDV datasets is lessened. The SBAS-derived results are negatively influenced because the pre-landslide

acceleration pattern is not well identified.

VI. Conclusion

Two primary issues are addressed using the multi-temporal (MT) spaceborne side-looking SAR observations and InSAR technique to monitor the slope stability in rugged terrains. First, geometric distortions can occur when a polar-orbit SAR images the area of interest (AOI), and the degree of distortions differs for ascending- or descending-orbit SAR observations. With the spaceborne observations, SAR incidence angle variation is small, not offering many options to resolve the geometric distortions. Therefore, the distortion assessment is critical, and the procedure coupled with the digital elevation model (DEM) is outlined to assess the criticality.

Second, a ground control point (GCP) in the SBAS analysis should be situated at a spatiotemporally stable location to correct orbital phase errors and derive ground surface displacements. As artificial targets are scarce and difficult to conduct fieldwork in remote mountainous areas, the GCP is primarily selected by analyzing the SAR and InSAR datasets. Thus, a valid and operational procedure for efficiently selecting GCPs is essential but yet to be developed. The studied GCP selection procedure is to fill in the void, and it is iterative and consists of four criteria. i) A GCP is at a location whose interferometric phase is consistent. The consistency is measured by the phase derivative variance (PDV) of an interferogram. Multiple interferograms are used to ensure the consistency throughout the InSAR data stack. ii) A GCP is at a location with temporal stability, and a small amplitude dispersion index (ADI) is considered. iii) Georeferencing SAR datasets in the InSAR analysis is a must operation and is achieved at the smallest increment of one row or column. Thus, a GCP should be at least within a patch of 2×2 pixels, with all four pixels being GCPs to minimize the georeferencing uncertainty. iv) GCPs should be spatially dispersed within the entire study area such that the InSAR outcomes are not biased by a single GCP or a single GCP cluster.

Showcasing the 2017 Xinmo landslide event, we evaluated the geometric distortions. The landslide impacted area was nearly entirely affected by foreshortening when the SAR observed the area along ascending orbits. The area was almost not distorted when the SAR observations were along descending orbits. At a ground-range resolution of 20×20 m, the tear-away zone had 309 pixels. With ascending-orbit Sentinel-1 SAR observations, 143 were impacted by foreshortening and 166 by the layover, or the entire zone was affected. The number of pixels without distortions was 156 (50.5%) with descending-orbit observations. Therefore, descending-orbit imaging is preferred.

To validate the proposed GCP selection method, we used the SBAS InSAR technique analyzing 45 descending-orbit SAR datasets. Setting the temporal baseline ≤ 96 days and spatial baseline ≤ 200 m, we obtained 155 differential interferograms. With the above four criteria to select GCPs, a subset of interferograms was randomly selected and used to evaluate the interferometric phase consistency with the PDV. The ADI was derived after aligning 45 amplitude images to assess the radar return's stability over time. Four GCP clusters were identified when the number of interferograms in the subset was 20, PDV ≤ 0.14, and ADI ≤ 0.20. The clusters were spatially dispersed within the study area. Then, one GCP per cluster was identified. With the four GCPs and SBAS InSAR technique, the phase ramp was corrected. The displacement and velocity values at three sample locations inside a stable area were obtained and studied. The values indicated they were steady within the period of interest. Then, the displacement and velocity values at three places within the tear-away zone were analyzed. The downward movement trends were clear, and accelerated movement patterns were evident before the landslide event. Thus, the proposed GCP selection method was validated since the InSAR-derived results were valid.

Acknowledgment

Sentinel-1 data©, Copernicus of European Space Agency (ESA) and DEM were downloaded from the http://vertex.daac.asf.alaska.edu/ of Alaska Satellite Facility, USA. The Landsat-8 images were downloaded from the USGS website, https://earthexplorer.usgs.gov.

References

[1] A. K. Gabriel, R. M. Goldstein, and H. A. Zebker, "Mapping small elevation changes over large areas: differential radar interferometry," *J. Geophys. Res. Solid Earth*, vol. 94, no. B7, pp. 9183-9191, Jul. 1989, doi: 10.1029/JB094iB07p09183.

[2] R. Bamler and P. Hartl, "Synthetic aperture radar interferometry," *Inverse Probl.*, vol. 14, no. 4, pp. R1–R54, Aug. 1998, doi: 10.1088/0266-5611/14/4/001.

[3] P. A. Rosen et al., "Synthetic aperture radar interferometry," *Proc. IEEE*, vol. 88, no. 3, pp. 333–382, Mar. 2000, doi: 10.1109/5.838084.

[4] L. Zhou, H. Yu, Y. Lan, and M. Xing, "Artificial intelligence in interferometric synthetic aperture radar phase unwrapping," *IEEE Geosci. Remote Sens. Mag.*, vol. 9, no. 2, pp. 10-28, Jun. 2021, doi: 10.1109/MGRS.2021.3065811.

[5] Z. Lu, E. Fielding, M. R. Patrick, and C. M. Trautwein, "Estimating lava volume by precision combination of multiple baseline spaceborne and airborne interferometric synthetic aperture radar: the 1997 eruption of Okmok volcano, Alaska," *IEEE Trans. Geosci. Remote Sens.*, vol. 41, no. 6, pp. 1428-1436, Jun. 2003, doi: 10.1109/TGRS.2003.811553.

[6] H. Liang, X. Li, and R.-F. Chen, "Mapping surface deformation over Tatun volcano group, northern Taiwan using multitemporal InSAR," *IEEE J. Sel. Top. Appl. Earth Observ. Remote Sens.*, vol. 14, pp. 2087-2095, 2021, doi: 10.1109/JSTARS.2021.3050644.

[7] T. Zeng, A. Ghula, W.-N Yang, M. Grzovic, and M. Maimaitiyiming, "Estimating the contribution of loose deposits to potential landslides over Wenchuan earthquake zone, China," *IEEE J. Sel. Top. Appl. Earth Observ. Remote Sens.*, vol. 8, no. 2, pp. 750-762, Feb. 2015, doi: 10.1109/JSTARS.2014.2349953.

[8] A. Novellino et al., "Slow-moving landslide risk assessment combining machine learning and InSAR techniques," *Catena*, vol. 203, Aug. 2021, Art. no. 105317, doi: 10.1016/j.catena.2021.105317.

[9] W. Qu et al., "Sentinel-1 InSAR observations of co- and post-seismic deformation mechanisms of the 2016 Mw 5.9 Menyuan earthquake, northwestern China," A*dv. Space Res*., vol. 68, no. 3, pp. 1301-1317, Aug. 2021, doi: 10.1016/j.asr.2021.03.016.

[10] M. Lazecky, I. Hlavacova, M. Bakon, J. J. Sousa, D. Perissin, and G. Patricio, "Bridge displacements monitoring using space-borne X-band SAR interferometry," *EEE J. Sel. Top. Appl. Earth Observ. Remote Sens.*, vol. 10, no. 1, pp. 205-210, Jan. 2017, doi: 10.1109/JSTARS.2016.2587778.

[11] D. H. T. Minh et al., "Measuring ground subsidence in Ha Noi through the radar interferometry technique using TerraSAR-X and Cosmos SkyMed data," *EEE J. Sel. Top. Appl. Earth Observ. Remote Sens.*, vol. 12, no. 10, pp. 3874-3884, Oct. 2019, doi: 10.1109/JSTARS.2019.2937398.

[12] D. Perissin and T. Wang, "Time-series InSAR application over urban areas in China," *IEEE J. Sel. Top. Appl. Earth Observ. Remote Sens.*, vol. 4, no. 1, pp. 92-100, Mar. 2011, doi: 10.1109/JSTARS.2010.2046883.

[13] Y. Chen, Y. Tong, and K. Tan, "Coal mining deformation using SBAS-InSAR and offset tracking: a case study of Yu County, China," *IEEE J. Sel. Top. Appl. Earth Observ. Remote Sens.*, vol. 13, pp. 6077-6087, 2020, doi: 10.1109/JSTARS.2020.3028083.

[14] L. Zhu, X. Xing, Y. Zhu, W. Peng, Z. Yuan, and Q. Xia, "An advanced time-series InSAR approach based on Poisson curve for soft clay highway deformation monitoring," *IEEE J. Sel. Top. Appl. Earth Observ. Remote Sens.*, vol. 14, pp. 7682-7698, 2021, doi: 10.1109/JSTARS.2021.3100086.

[15] Y. Wang et al., "Using TerraSAR X-band and Sentinel-1 C-band SAR interferometry for deformation along Beijing-Tianjin intercity railway analysis," *IEEE J. Sel. Top. Appl. Earth Observ. Remote Sens.*, vol. 14, pp. 4832-4841, 2021, doi: 10.1109/JSTARS.2021.3076244.

[16] M. D. Soldato, L. Solari, A. Novellino, O. Monserrat, and F. Raspini, "A new set of tools for the generation of InSAR visibility maps over wide areas," *Geosciences*, vol. 11, no. 6, May. 2021, Art. no. 229, doi: 10.3390/geosciences11060229.

[17] A. Ferretti, C. Prati, and F. Rocca, "Permanent scatterers in SAR interferometry," *IEEE Trans. Geosci. Remote Sens*., vol. 39, no. 1, pp. 8-20, Jan. 2001, doi: 10.1109/36.898661.

[18] P. Berardino, G. Fornaro, R. Lanari, and E. Sansosti, "A new algorithm for surface deformation monitoring based on small baseline differential SAR interferograms," *IEEE Trans. Geosci. Remote Sens*., vol. 40, no. 11, pp. 2375-2383, Nov. 2002, doi: 10.1109/TGRS.2002.803792.

[19] A. Pepe, G. Solaro, F. Calo, and C. Dema, "A minimum acceleration approach for the retrieval of multiplatform InSAR deformation time series," *IEEE J. Sel. Top. Appl. Earth Observ. Remote Sens.*, vol. 9, no. 8, pp. 3883-3898, Aug. 2016, doi: 10.1109/JSTARS.2016.2577878.

[20] R. Shamshiri, H. Nahavandchi, and M. Motagh, "Persistent scatterer analysis using dual-polarization Sentinel-1 data: contribution from VH channel," *IEEE J. Sel. Top. Appl. Earth Observ. Remote Sens*., vol. 11, no. 9, pp. 3105-3112, Sep. 2018, doi: 10.1109/JSTARS.2018.2848111.

[21] C. Zhao, Z. Li, B. Tian, P. Zhang, and Q. Chen, "A ground surface deformation monitoring InSAR method using improved distributed scatterers phase estimation," *IEEE J. Sel. Top. Appl. Earth Observ. Remote Sens.*, vol. 12, no. 11, pp. 4543-4553, Nov. 2019, doi: 10.1109/JSTARS.2019.2946729.

[22] R. F. Hanssen, "Stochastic model for radar interferometry" in *Radar interferometry: data interpretation and error analysis*. Norwell, MA: Kluwer, 2001, pp. 113-132.

[23] M. Shirzaei and T. R. Walter, "Estimating the effect of satellite orbital error using wavelet-based robust regression applied to InSAR deformation data," *IEEE Trans. Geosci. Remote Sens*., vol. 49, no. 11, pp. 4600-4605, Nov. 2011, doi: 10.1109/TGRS.2011.2143419.

[24] N. Gourmelen, F. Amelung, and R. Lanari, "Interferometric synthetic aperture radar–GPS integration: interseismic strain accumulation across the Hunter mountain fault in the eastern California shear zone," *J. Geophys. Res. Solid Earth*, vol. 115, Sep. 2010, Art. no. B09408, doi: 10.1029/2009JB007064.

[25] Y. Fialko, "Interseismic strain accumulation and the earthquake potential on the southern San Andreas fault system," *Nature*, vol. 441, no. 7096, pp. 968-971, Jun. 2006, doi: 10.1038/nature04797.

[26] P. Lundgren, E. A. Hetland, Z. Liu, and E. J. Fielding, "Southern San Andreas-San Jacinto fault system slip rates estimated from earthquake cycle models constrained by GPS and interferometric synthetic aperture radar observations," *J. Geophys. Res*., vol. 114, 2009, Art. no. B02403, doi: 10.1029/2008JB005996.

[27] M. D. Pritt, "Phase unwrapping by means of multigrid techniques for interferometric SAR," *IEEE Trans. Geosci. Remote Sens*., vol. 34, no. 3, pp. 728-738, May. 1996, doi: 10.1109/36.499752.

[28] D. C. Ghiglia and M. D. Pritt, "Phase data, quality maps, masks, and filters," in *Two-dimensional Phase Unwrapping: Theory, Algorithm, and Software*. New York, NY, USA: Wiley, 1998, pp. 59-99.

[29] E. Intrieri et al., "The Maoxian landslide as seen from space: detecting precursors of failure with Sentinel-1 data," *Landslides*, vol. 15, no. 1, pp. 123-133, Jan. 2018, doi: 10.1007/s10346-017-0915-7.

[30] J. Dong et al., "Measuring precursory movements of the recent Xinmo landslide in Mao County, China with Sentinel-1 and ALOS-2 PALSAR-2 datasets," *Landslides*, vol. 15, no. 1, pp. 135-144, Jan. 2018, doi: 10.1007/s10346-017-0914-8.

[31] Y. Kang, Z. Lu, C. Zhao, Q. Zhang, J.-W. Kim, and Y. Niu, "Diagnosis of Xinmo (China) landslide based on interferometric synthetic aperture radar observation and modeling," *Remote Sens*., vol. 11, no. 16, Aug. 2019, Art. no. 1846, doi: 10.3390/rs11161846.

[32] F. Raspini, E. Intrieri, D. Festa, and N. Casagli. "Landslide mapping and monitoring with satellite interferometry," in *Understanding and Reducing Landslide Disaster Risk*. Gewerbestrasse, Cham, Switzerland: Springer Nature Switzerland AG., 2021, pp. 149-154.

[33] Y. Yan and Y. Wang, "An effective approach to select valid and accurate ground control points in SBAS-InSAR technique," in *Proc. Eur. Conf. Syn. Aperture Radar*, Germany, 2021, pp. 829-832.